ChemCatChem

Research Article
doi.org/10.1002/cctc.202501017

Chemistry Europe
European Chemical Societies Publishing

www.chemcatchem.org

Cu-SSZ-13 Catalysts Designed Through Interzeolite Conversion Process From Different Structure Types of Zeolites for NH_3-SCR-DeNO$_x$: Structure-Property Activity Relationships and Intermediates Determination

Alejandro Mollá Robles,[a] Magdalena Jabłońska[†],*[a] Ana Palčić,[b] Matej Bubaš,[c] Jie Yang,[d] Marek Rotko,[e] Muhammad Fernadi Lukman,[f] Anqi Guo,[g] Marko Bertmer,[f] Matej Huš,[h] Junjiang Zhu,[d] Ulrich Simon,[g] Andreas Pöppl,[f] and Nataša Novak Tušar[c]

The intermediates and their respective role in reduction and oxidation cycles in the selective catalytic reduction of NO$_{xx}$ with ammonia reaction mechanism (NH_3-SCR-DeNO$_x$) are widely and controversially discussed. To finally clear up the discussion, a variety of Cu-containing CHA structure type zeolites (Cu-SSZ-13) were prepared using different zeolite sources, such as MFI, BEA and FAU structure type zeolites. Cu-SSZ-13 prepared samples were investigated as catalysts for NH_3-SCR-DeNO$_x$. The structure-property-activity relationship of the Cu-SSZ-13 prepared samples varied depending on the applied initial zeolite. Cu-SSZ-13 catalysts prepared from MFI and BEA structure types of zeolites are more N_2 selective than Cu-SSZ-13 catalysts prepared from FAU structure type of zeolite. In situ spectroscopy, temperature-programmed and transient techniques supported by density functional theory (DFT) were used to investigate the reaction mechanism and confirmed the intermediates of the reduction- and oxidation-half cycles: NH_4^+, NH_x^-, $[(NH_3)_4Cu^{II}{}_2O_2]^{2+}$, NO_2^-/NO_3^- species. The SCR paths involved determine that the dominant reaction occurs between adsorbed NH_3 on the catalyst surface and NO from the gas phase, as well as the reaction between adsorbed NO_x^- (nitrites/nitrates) and NH_3.

1. Introduction

The versatility of zeolites has allowed for their application in diverse fields, from processes such as ion exchange and molecular sieving to heterogeneous catalysis or drug delivery.[1] One such field is emission control, where zeolites (most notoriously CHA-type zeolites, due to their advantages, e.g., small-pore structure, thermal stability, etc.) have been used in diesel exhaust gas systems for the selective catalytic reduction of nitrogen oxides into nitrogen and water vapor, using ammonia as a reductant (NH_3-SCR-DeNO$_x$).[2] In addition to that, transition metals (e.g., iron, copper, manganese, etc.) have been broadly investigated as active sites for this reaction, while Cu^{2+} and Fe^{3+} are considered the most active and selective towards the formation of N_2.[3] SSZ-13 is a zeolite with a CHA-type framework composed of two building blocks, a double six-ring and a chabazite cage. The framework building blocks are formed by four-, six- (6MRs), and eight-membered rings (8MRs). The eight-member ring pore opening to the *cha* cage cavity is 0.38 × 0.38 nm in size; thus, SSZ-13 is considered a small-pore zeolite. The introduction

[a] *A. M. Robles, M. Jabłońska[†]*
Institute of Chemical Technology, Universität Leipzig, Linnéstr. 3 04103, Leipzig, Germany
E-mail: magdalena.jablonska@uni-leipzig.de

[b] *A. Palčić*
Laboratory for the Synthesis of New Materials, Division of Materials Chemistry, Ruđer Bošković Institute, Bijenička 54, Zagreb 10000, Croatia

[c] *M. Bubaš, N. N. Tušar*
Laboratory for Catalysts, Department of Inorganic Chemistry and Technology, National Institute of Chemistry, Ljubljana SI-1000, Slovenia

[d] *J. Yang, J. Zhu*
Hubei Key Laboratory of Biomass Fibers and Eco-dyeing and Finishing, College of Chemistry and Chemical Engineering, Wuhan Textile University, Wuhan 430200, China

[e] *M. Rotko*
Department of Chemical Technology, Institute of Chemical Sciences, Faculty of Chemistry, Maria Curie-Sklodowska University, 3 Maria Curie-Sklodowska Sq., Lublin 20031, Poland

[f] *M. F. Lukman, M. Bertmer, A. Pöppl*
Felix Bloch Institute for Solid State Physics, Universität Leipzig, Linnéstr. 5 04103, Leipzig, Germany

[g] *A. Guo, U. Simon*
Institute of Inorganic Chemistry, RWTH Aachen University 52074, Aachen, Germany

[h] *M. Huš*
Department of Catalysis and Chemical Reaction Engineering, National Institute of Chemistry, Ljubljana SI-1000, Slovenia

[†] *University of Łódź, Faculty of Chemistry, Department of Inorganic and Analytical Chemistry, Tamka 12, 91–403 Łódź, Poland*

Supporting information for this article is available on the WWW under https://doi.org/10.1002/cctc.202501017

of cations (e.g., Cu^{2+}) balances out the charge difference that framework Al creates. Cu^{2+} ions are mainly located in 6MRs neutralizing the negative charges of two Al sites, while $[Cu(OH)]^+$ are predominantly located in 8MRs neutralizing the negative charge of a single Al site.[4,5] The quantity of ions in these two locations depends on different parameters (i.e., Cu loading, *n*(Si)/*n*(Al) ratio and *n*(Cu)/*n*(Al) ratio).

The NH_3-SCR-DeNO$_x$ reaction mechanism consists of both a reduction ($Cu^{2+} \rightarrow Cu^+$) and an oxidation ($Cu^+ \rightarrow Cu^{2+}$) half-cycles. The reduction of copper species takes place under its exposure to both NH_3 and NO, while oxidation occurs in the presence of O_2 (NO is considered not relevant for the catalyst re-oxidation at low temperatures).[6,7] For the reduction half-cycle, mainly mixed NO-associated complexes (i.e., $Cu^{II}(OH)(NH_3)_{n-1}(NO)]^+$)[8,9] or HONO intermediates[10,11] are considered. The HONO-based low-temperature reduction half-cycle mechanism was proposed to proceed via a reaction of NO with a pair of Cu^{2+} sites (e.g., Cu dimers or two proximate - *Two-P*, $[Cu^{II}(OH)(NH_3)_3\ldots Cu^{II}(OH)(NH_3)_3]$). The formed HONO and $[Cu^{I}(NH_3)_2]^+$ react together with the formation of NH_4NO_2, finally decomposing to N_2 and H_2O.

For the oxidation half-cycle μ-η^2,η^2-peroxo diamino dicopper $[Cu^{II}_2O_2(NH_3)_4]^{2+}$ and nitrates are considered as the reaction intermediates. The $[Cu^{II}_2O_2(NH_3)_4]^{2+}$ peroxo complexes are formed over Cu-containing SSZ-13 in a reaction between O_2 and two mobile linear $[Cu^{I}(NH_3)_2]^+$ complexes, which come into contact by migrating from their respective cationic sites into the chabazite cage.[12] Besides Cu-containing SSZ-13, the formation of $[Cu^{II}_2O_2(NH_3)_4]^{2+}$ complexes and thus, the oxidation half-cycle was confirmed for other Cu-containing zeolites, such as ZSM-5, Y, and ERI.[13,14] On the other hand, the mechanism associated with the reduction of the $[Cu^{II}_2O_2(NH_3)_4]^{2+}$ peroxo complex is widely discussed (e.g.,[7,15]). Our last studies revealed an enhanced capacity to generate a greater quantity of Cu dimer species during NH_3-SCR-DeNO$_x$ over Cu-SSZ-13 (compared to Cu-ERI and Cu-ZSM-5). This observation aligns with its superior activity below 200 °C.[13] The reaction of NO with the peroxo complex governs the NH_3-SCR-DeNO$_x$ activity. This conclusion aligns with previous findings for Cu-containing SSZ-13, which demonstrate an enhanced activity for NH_3-SCR-DeNO$_x$.[16] Negri et al.[17] have confirmed the complete reduction of the $[Cu^{II}_2O_2(NH_3)_4]^{2+}$ peroxo complex in a mixture of NO and NH_3 to the linear $[Cu^{I}(NH_3)_2]^+$ using in situ XAS, indicating that the NH_3-SCR-DeNO$_x$ activity is determined by this reaction step. On the other side, Nasir et al.[18] claimed that Cu-NO_3 species are key intermediates in the oxidizing step of Cu(I)-CHA in the presence of gaseous NO and O_2. Furthermore, taking into account that NH_3 first fills the copper coordination sphere for the oxidation half-cycle, mixed NO_x^--associated complexes (i.e., $[Cu^{II}(NH_3)_3(NO_3)]^+$) are considered. Such complexes are approved via FT-IR, DR UV-vis, and EXAFS spectroscopy as well as via density functional theory (DFT) calculations.[9,19] Overall, the lack of an established mechanism hinders the rational design of catalysts for improving the NH_3-SCR-DeNO$_x$ activity, N_2 selectivity and stability.

Zeolite SSZ-13 (CHA structure type) is often prepared via interzeolite conversion using FAU-type zeolites as a parent material.[20,21] In our previous studies, we reported a series of CHA structure-type materials prepared from FAU-type zeolite by reducing the amount of structure-directing agent (i.e., *N,N,N*-trimethyl-1-adamantammonium hydroxide, TMAdaOH).[22] Taking this into consideration, it was found that the properties of the initial reaction mixture in the interzeolite conversion process, analogously as in the other zeolite synthesis paths, affect the material properties and, consequently, the catalytic properties of the resulting daughter zeolite.[23,24]

The reaction intermediates and their respective role in the reduction and oxidation cycles of the NH_3-SCR-DeNO$_x$ reaction are widely and controversially discussed, indicating difficulty in the validation of a detailed DFT modelling with experimental data. For this study, a set of Cu-SSZ-13 zeolite samples (CHA structure type) was designed and developed to employ different starting zeolite materials (i.e., FAU, BEA, MFI). Thus, the novelty of the studies is manifested in the systematic application and comparison of interzeolite conversion from different parent zeolite materials under tailored synthesis conditions - offering new insights into how precursor choice affects final catalyst properties. The final materials in their Cu-forms have been physico-chemically characterized and evaluated for their activity and N_2 selectivity in NH_3-SCR-DeNO$_x$. The mechanistic aspects of the reaction were explored via spectroscopic, temperature-programmed and transient techniques supported by modelling to gain a better understanding of the impact of the involved reaction intermediates on the catalytic properties of the investigated Cu-CHA materials.

2. Experimental Section

2.1. Catalyst Preparation

Chabazite-type zeolite samples (CHA) were prepared via interzeolite conversion using commercial MFI- (IRZ-MFI001 – H-form, *n*(Si)/*n*(Al) = 12, International Reference Zeolite material provided by the Catalysis Commission of International Zeolite Association, produced by Tosoh; CBV3024E – NH_4^+-form, Zeolyst), BEA- (CBV814E – NH_4^+-form, *n*(Si)/*n*(Al) = 30, Zeolyst) and FAU-type (CBV760 – H^+-form, *n*(Si)/*n*(Al) = 30, Zeolyst) zeolite materials, sodium hydroxide (NaOH, pellets, 97 wt.%, Acros organics), potassium hydroxide (KOH, flakes, 89 wt.%, Gram-mol.) *N,N,N*-trimethyl-1-adamantammonium hydroxide (TMADAOH, 20 wt.% solution, Sachem) and doubly distilled water. Prior to the synthesis, the materials in NH_4^+-form (CBV3024E and CBV814E) were converted to H^+-form through calcination at 450 °C (1.42 °C min^{-1}, 5 h). The required quantities of the chemicals were mixed in order to achieve the molar oxide compositions of the synthesis mixtures listed in Table 1. These mixtures were charged into polyterafluoroethene (PTFE) lined steel autoclaves and hydrothermally treated at 150 °C for a given period of time. The final product was recovered by centrifugation, washed repeatedly until the pH value of the supernatant had reached 7, and dried in a convection oven at 80 °C. Thus, the obtained CHA-type zeolite materials were calcined at 600 °C for 6 h in static air, 1 °C min^{-1}, afterwards they were subjected to a 3-fold ion exchange in an aqueous solution (0.5 M) of ammonium nitrate (> 99 wt.%, Merck) at 60 °C for 1 h, the resulting slurry was filtrated, washed and dried. Subsequently, the solids were ion-exchanged in a solution (0.05 M) of copper acetate ($Cu(OOCCH_3)_2$, (≥ 98 wt.%, anhydrous, Alfa Aesar)

Table 1. Synthesis parameters of the samples.

Sample	Reaction Mixture Composition	Time / d	Source
SSZ-13_MFI_1	1 SiO_2: 0.042 Al_2O_3: 0.25 KOH: 0.125 TMAdaOH: 15 H_2O	30	MFI - IRZ-MFI001
SSZ-13_MFI_2	1 SiO_2: 0.042 Al_2O_3: 0.125 KOH: 0.125 TMAdaOH: 15 H_2O	30	MFI - IRZ-MFI001
SSZ-13_MFI_3	1 SiO_2: 0.042 Al_2O_3: 0.25 NaOH: 0.25 TMAdaOH: 15 H_2O	30	MFI - IRZ-MFI001
SSZ-13_MFI_4	1 SiO_2: 0.042 Al_2O_3: 0.125 NaOH: 0.125 TMAdaOH: 15 H_2O	30	MFI - IRZ-MFI001
SSZ-13_MFI_5	1 SiO_2: 0.0167 Al_2O_3: 0.25 NaOH: 0.125 TMAdaOH: 15 H_2O	12	MFI - CBV3024E
SSZ-13_BEA_6	1 SiO_2: 0.042 Al_2O_3: 0.25 NaOH: 0.125 TMAdaOH: 15 H_2O	6	BEA - CBV814E
SSZ-13_FAU_7	1 SiO_2: 0.0167 Al_2O_3: 0.25 NaOH: 0.125 TMAdaOH: 15 H_2O	12	FAU - CBV760

for 24 h at room temperature. Afterwards, the product was separated by filtration and thoroughly washed. The obtained materials were dried at room temperature. Finally, the solids were calcined at 600 °C for 6 h with a heating rate of 1 °C min^{-1}. Table 1 gathers sample names, preparation conditions and applied precursors.

2.2. Catalyst Characterization and Catalytic Experiments

The prepared Cu-containing CHA type zeolites have been thoroughly physico-chemically characterized through powder X-ray diffraction (XRD), N_2 sorption, inductively coupled plasma optical emission spectroscopy (ICP-OES), scanning electron microscopy (SEM), solid-state nuclear magnetic resonance (NMR), diffuse reflectance UV–vis spectroscopy (DR UV–vis), temperature programmed reduction with H_2 (H_2-TPR), electron paramagnetic resonance (EPR). The mechanistic aspects, i.e., reduction-oxidation half-cycles over applied catalysts, were evaluated by in situ diffuse reflectance infrared Fourier transform spectroscopy (in situ DRIFTS) and time-resolved in situ FT-IR, in situ impedance spectroscopy (in situ IS), in situ diffuse reflectance UV–vis spectroscopy (in situ DR UV–vis), catalytic experiments, as well as temperature-programmed studies, steady-state isotopic transient kinetic analysis (SSITKA), and DFT modelling.

Details concerning physico-chemical characterization, catalytic experiments and modelling can be found in the Supplementary Information.

3. Results and Discussion

3.1. Structural and Textural Properties

Figure 1a,b shows the X-ray diffraction profiles of the protonic form of zeolites and respective Cu-containing materials. All samples exhibit patterns characteristic of a chabazite (CHA) framework (with 2θ = 9.5°, 12.9°, 16.2°, 18.0°, 20.8°, 25.3°, 26.2°, 30.9°, 31.5°).[25] In addition to that, no reflections related to crystals of copper oxides (e.g., 2θ = 35°, 39°)[26] are present in the profiles of the Cu-containing SSZ-13. The N_2 sorption isotherms of the Cu-containing zeolites (Figures 1c and S1) can be classified as type I, which is characteristic of microporous materials.[27] However, the Cu-SSZ-13_FAU_7 sample exhibits a higher specific adsorbed volume at high relative pressures, as compared to the other samples. Moreover, Cu-SSZ-13_FAU_7 possesses a specific mesopore volume one order of magnitude greater than the rest of the samples (Table S1), which could be explained by the sample exhibiting the smallest particle size (SEM images in Figure 2, Table S2) and consequently larger interparticle volume. These claims are also backed by the pore width distribution of the samples, all the catalysts are predominantly microporous (Figure 1d), although Cu-SSZ-13_FAU_7 displays a higher derivative of the adsorbed volume than the other materials. This data stays in line with our previously investigated Cu-containing CHA samples.[22]

The SEM analysis performed to study both the size and morphology of the zeolite particles (Figure 2) shows that these can be considered as cubic-shaped, although intergrowth also occurs. Furthermore, the size of the particles was also evaluated through this technique (Table S2). The samples Cu-SSZ-13_MFI_1, Cu-SSZ-13_MFI_5, Cu-SSZ-13_BEA_6, and Cu-SSZ-13_FAU_7 have an average size between 1555, 1430, 1048, and 196 nm, while the samples Cu-SSZ-13_MFI_2 and Cu-SSZ-13_MFI_3 possess an average particle size between 8643 and 7696 nm, respectively (Figure 2b,c). Finally, the sample Cu-SSZ-13_MFI_4 exhibits the biggest particles with an average size of 20,489 nm. The differences in particle sizes appeared due to the changes in the reaction mixture composition for each zeolite synthesis, i.e., the properties of the starting zeolite employed. Moreover, a higher content of hydroxide ions in the reaction mixture leads to the generation of more nuclei from where crystals can grow, resulting in smaller crystal sizes.[22] Furthermore, a distinction can be made regarding the homogeneity of particle sizes. The samples Cu-SSZ-13_MFI_5, Cu-SSZ-13_BEA_6, and Cu-SSZ-13_FAU_7 possess a particle size with uniform monomodal distribution and a smaller variability in particle size. However, for the other catalysts, we can observe in the SEM images a bimodal particle distribution in which two different groups of particles with different sizes are present. Moreover, for Cu-SSZ-13_MFI_3 and Cu-SSZ-13_MFI_4, the presence of shard-like particles can be detected. Clearly, there is a difference in the distribution of zeolite growth species in each system, both in terms of the time of their appearance and also in their concentration. Two groups of particles having significantly different crystal sizes in Cu-SSZ-13_MFI_1 suggest that two populations of nuclei were formed in the system. Larger crystals started to grow in the earlier stage of the reaction, while the onset of the growth of the smaller particles began later in the reaction. Further, the amount of particles in each fraction indicates the number of nuclei formed in the course of the preparation of SSZ-13 materials. However, a thorough discussion on this matter is out of the scope of this paper.

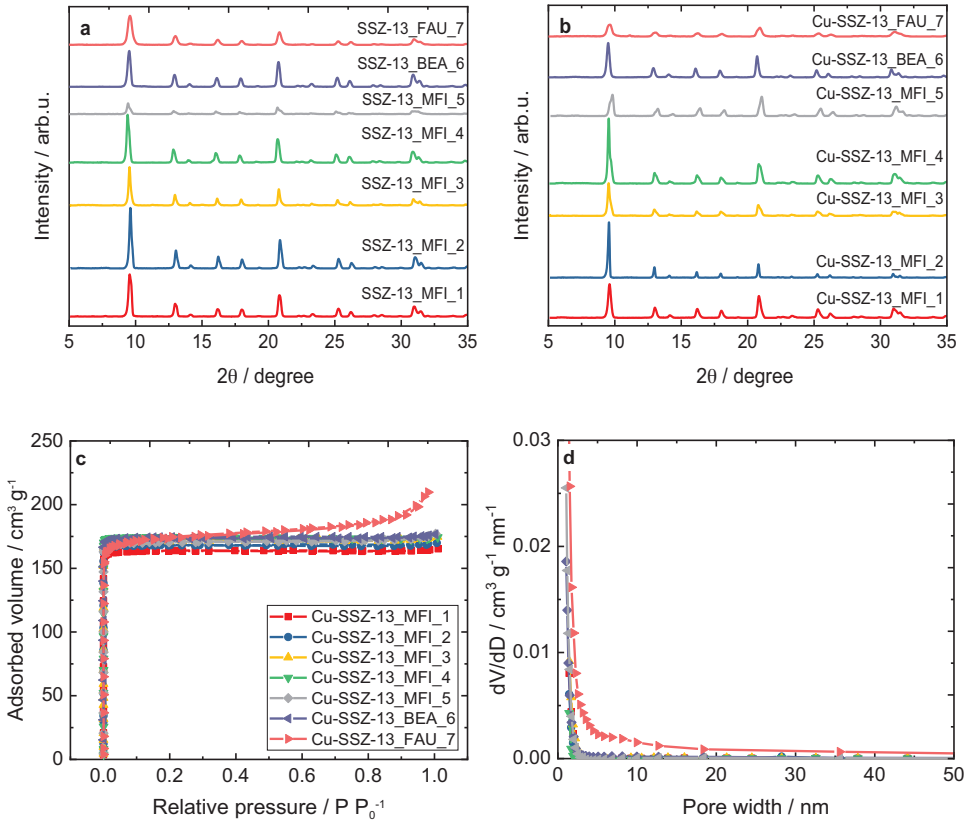

Figure 1. XRD patterns of a) calcined SSZ-13 samples and b) their Cu-containing form. Sample labels as in Table 1 as well as c) N_2 sorption isotherms and d) pore width distribution of the Cu-containing SSZ-13; see Figure S1 for the separate spectra.

Table 2. Results of the elemental analysis of the Cu-containing SSZ-13 samples (ω_i: mass fractions).

Sample	ω_{Si} / wt.%	ω_{Al} / wt.%	ω_{Cu} / wt.%	n(Si)/n(Al)	n(Cu)/n(Al)
Cu-SSZ-13_MFI_1	40.70	4.08	2.59	9.58	0.27
Cu-SSZ-13_MFI_2	40.60	3.40	1.81	11.54	0.23
Cu-SSZ-13_MFI_3	40.10	4.85	1.67	7.94	0.15
Cu-SSZ-13_MFI_4	42.60	3.70	0.96	11.10	0.11
Cu-SSZ-13_MFI_5	40.10	3.83	3.59	10.10	0.40
Cu-SSZ-13_BEA_6	38.80	4.29	3.41	8.69	0.34
Cu-SSZ-13_FAU_7	41.20	2.37	4.72	16.70	0.85

The analysis of the chemical composition of the samples (Table 2) shows that the materials possess a n(Si)/n(Al) ratio between 7.94 and 11.54, with the exception of Cu-SSZ-13–7, with a n(Si)/n(Al) ratio of 16.70. All samples exhibit a value of n(Cu)/n(Al) ratio lower than 0.5, again except Cu-SSZ-13_FAU_7, whose n(Cu)/n(Al) ratio is 0.85. Considering that copper balances out the negative charges of the Al in the zeolite framework, a n(Cu)/n(Al) = 0.5 means that all the Al charges have been compensated. However, if the amount of copper surpasses that value, the excess can be converted through calcination into copper oxide species located on the external surface of zeolite grains. The differences in copper content can be attributed to the different particle sizes that the zeolites possess, smaller particles have a more available specific surface area that can interact with the copper solution during the ion exchange.[22] Thus, that trend can be seen in the seven samples (Figure 2h). Moreover, the presence of different size distributions can also affect the copper loading of the samples. The materials that exhibit bimodal particle distributions possess bigger crystals, which can lead to a lower amount of deposited copper. According to our previous studies,[22] Cu-containing SSZ-13 based on FAU zeolite possessed a Cu loading of 4.4–5.2 wt.%.

In order to investigate the differences in Al and Si coordination between the samples, ^{29}Si and ^{27}Al solid-state NMR was applied (Figures S2 and S4, Tables S3 and S4). ^{29}Si solid-state NMR serves to identify the distribution of silicon and aluminum atoms, considering a central SiO_4 unit that can be surrounded by four atoms (Si or Al). Out of the five possible coordination struc-

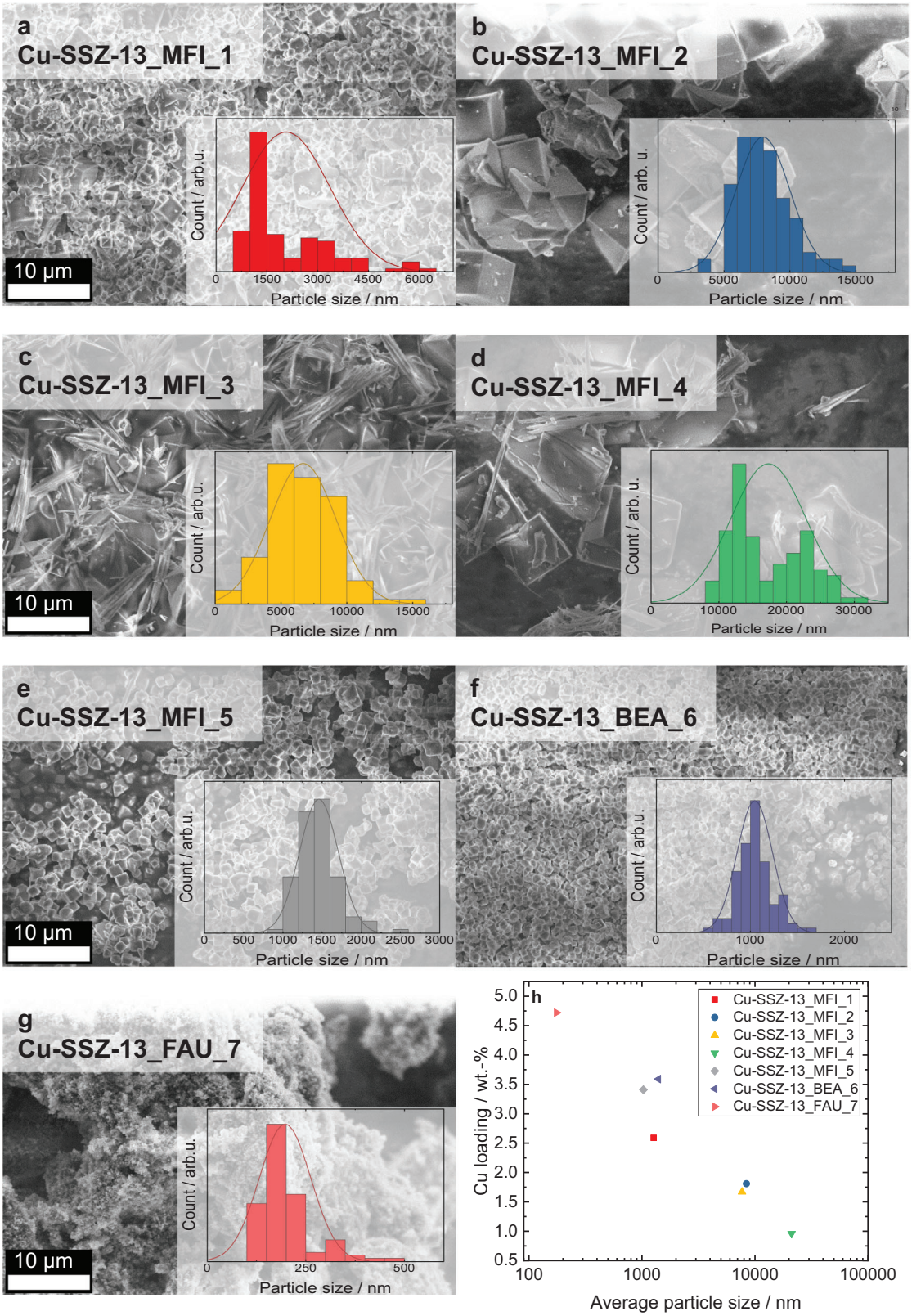

Figure 2. SEM images of the Cu-containing SSZ-13 samples: a) Cu-SSZ-13_MFI_1, b) Cu-SSZ-13_MFI_2, c) Cu-SSZ-13_MFI_3, d) Cu-SSZ-13_MFI_4, e) Cu-SSZ-13_MFI_5, f) Cu-SSZ-13_BEA_6, g) Cu-SSZ-13_FAU_7, h) average particle size of Cu-containing SSZ-13 samples evaluated via counting 100 particles randomly from SEM images.

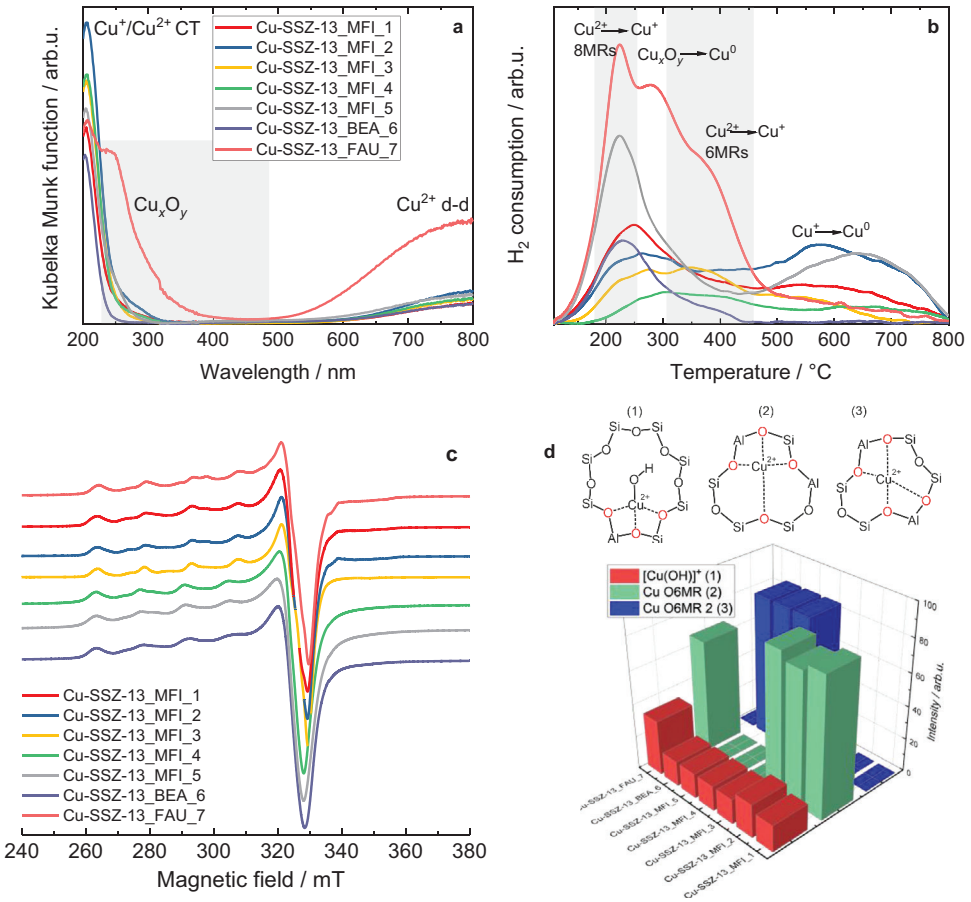

Figure 3. a) DR UV–vis spectra and b) H_2-TPR profiles of the Cu-containing SSZ-13 samples; a and b) sample labels are the same; c) cw-EPR spectra for the activated Cu-containing SSZ-13 samples at −196 °C, d) the percentage of Cu^{2+} speciation derived from the spectral simulation of the samples.

tures of Si(*n*Al) ($n = 0, 1, 2, 3, 4$), the main coordination structures that can be identified are Si(2Si,2Al), Si(3Si,1Al), and Si(4Si,0Al) which are ascribed to the resonances at −105 ppm, −107 ppm, −111 ppm, and −112 ppm, respectively. The most prominent one being Si(4Si,0Al), best deconvoluted by two sites (Figure S2c), followed by Si(3Si,1Al), and Si(2Si,2Al). Figure S2c,d show examples of the deconvolution for ^{29}Si and ^{27}Al NMR, respectively, while Figure S4 shows the schematic of the coordination environments of Si and Al. Regarding the results of the ^{27}Al solid-state NMR, only two signals have been identified, corresponding to Al atoms in tetrahedral (four-coordinated aluminum, Al^{IV}) and octahedral coordination (six-coordinated aluminum, Al^{VI}), Figure S2d. Lowenstein's rule forbids the possibility of an Al–O–Al pairing, which explains why Al in the zeolite framework can only be surrounded by Si atoms in a tetrahedral coordination.[28] Moreover, extraframework aluminum is detected as octahedral AlO_6 coordination. However, there is no significant difference in the coordination of Al and Si between the catalysts.

3.2. Nature of Copper Species

The copper speciation of the samples was analyzed through DR UV–vis spectroscopy (Figure 3a). The spectra showed that all of the samples exhibit two distinct bands between 200–250 nm and above 600 nm. The first band is related to the ligand-to-metal charge transfer (LMCT) between isolated Cu^{2+} and oxygen from the zeolite framework, and the second band (600–800 nm) arises due to the d–d transition of isolated Cu^{2+} species. Moreover, the Cu-SSZ-13_FAU_7 sample exhibits an additional band between 250–300 nm, which is related to the presence of copper oxide species.[5,29] The reduction profiles (Figure 3b) display a peak present in all the samples located between 200 and 250 °C, which relates to the reduction of Cu^{2+} located in 8MRs to Cu^{+}. Moreover, at around 350 °C, a peak also appears, correlated with the reduction of Cu^{2+} in 6MRs into Cu^{+}. Furthermore, at 550–600 °C, another peak can be seen associated with the reduction of Cu^{+} into Cu^{0}.[30] For the Cu-SSZ-13_FAU_7 sample, the reduction peak centered at 280 °C appeared due to the reduction of Cu_xO_y species to Cu^{0}.[22] This phenomenon is in line with the ICP data (Table 2), which shows that the *n*(Cu)/*n*(Al) ratio of Cu-SSZ-13_FAU_7 is 0.85, thus supporting the hypothesis of the presence of Cu_xO_y in this sample, which is, however, amorphous. Paolucci et al.[6] demonstrated through DFT and stochastic modelling that Cu ions prefer to be located in 6MRs with two Al sites. Thus, Cu ions first populate the sites in 6MRs until they are saturated; after that, they can become cationic sites in 8MRs. Moreover, they also modelled the fraction of$[Cu(OH)]^{+}$ as a function of both the *n*(Cu)/*n*(Al) ratio and *n*(Si)/*n*(Al) ratio. As the *n*(Si)/*n*(Al) increases, a lower quantity of copper is needed to

reach a higher fraction of $[Cu(OH)]^+$ with respect to the total loading of copper. This behavior can be explained by the position in which the $[Cu(OH)]^+$ ions are located. As the amount of Al decreases, the number of 6MRs with two Al sites diminishes; thus, the amount of copper needed to fully populate the 6MRs will be lower, and the remaining copper cations can populate 8MRs as $[Cu(OH)]^+$. Consequently, a low n(Si)/n(Al) ratio and low copper loading favor the formation of Cu^{2+} in 6MRs, while a high n(Si)/n(Al) ratio and high copper loadings favor the formation of $[Cu(OH)]^+$.[4] Furthermore, the N_2O decomposition over the investigated samples revealed that the highest conversion was achieved by Cu-SSZ-13_FAU_7, followed by Cu-SSZ-13_MFI_5 (Figure S5), which further supports the presence of Cu_xO_y in these samples. According to literature (e.g.,[31,32]), the enhanced catalytic activity for N_2O decomposition over copper-based mixed metal oxides has also been proved, while bulk CuO is inactive. Figure S6 shows the normalized concentration of the main compounds ($^{16}O_2$, $^{16}O^{18}O$, and $^{18}O_2$) during the temperature-programmed isotopic experiments (TPIE) over Cu-SSZ-13_MFI_2 and Cu-SSZ-13_BEA_6. The results indicate that in the temperature range corresponding to the NH_3-SCR-DeNO$_x$ process, there is no oxygen exchange between the gas phase and the crystal lattice of the catalysts. Therefore, it can be concluded that oxygen originating from the zeolite framework probably does not play a significant role in the NH_3-SCR-DeNO$_x$ process.

cw-EPR spectroscopy has been vastly employed to study the coordination environment of Cu^{2+} species (d^9, $S = \frac{1}{2}$ coupled to both copper isotopes ^{63}Cu and ^{65}Cu with nuclear spin $I = 3/2$) as an extraframework species in chabazite structure.[33,34] It is also known that the location of Cu^{2+} species or its coordination environment will depend on multiple factors, some of them are thermal activation, the properties of zeolites (e.g., n(Si)/n(Al) ratio and topology) and the extent of the ion exchange process.[34,35] At the hydrated state, all Cu-SSZ-13 samples measured at −196 °C possess relatively similar EPR spectral patterns dominated by $[Cu(H_2O)_6]^{2+}$ species with the EPR parameter $g_{zz} = 2.395$ and $A_{zz} = 440$ MHz as deduced from the simulation (Figure S7) except for Cu-SSZ-13_MFI_2 and Cu-SSZ-13_MFI_4 samples, which also have a contribution of another species (around 40%) with the EPR parameter $g_{zz} = 2.33$ and $A_{zz} = 390$ MHz.

Figure 3c displays all experimental spectra of the activated Cu-containing SSZ-13 samples, whereas their respective EPR simulation is given in Figure S8, Tables S5 and S6. Sample Cu-SSZ-13_FAU_7 exhibits the largest content of $[Cu(OH)]^+$ species, Cu^{2+} with one OH group and three zeolitic O species at 8MR position (Table S7 for detailed EPR parameter)[33] with $g_{zz} = 2.291$ and $A_{zz} = 410$ MHz and approximately 33% of the EPR spectra (Figure S8g). These species are often observed when the n(Si)/n(Al) ratio is higher than 11 (consequently lower amount of Al).[33] The rest of the signal (67%) can be attributed to the Cu O-6MR species (Cu^{2+} in a distorted tetragonal planar coordination in the six-membered ring position) with $g_{zz} = 2.353$ and $A_{zz} = 480$ MHz. Interestingly, Cu-SSZ-13_MFI-1(2,3) and Cu-SSZ-13_FAU_7 contain Cu O-6MR species as the major component of their EPR spectra, while Cu-SSZ-13_MFI_4(5) and Cu-SSZ-13_BEA_6 contain Cu O-6MR-2 species with simulated EPR parameters of $g_{zz} = 2.370$ and $A_{zz} = 440$ MHz. The Cu O-6MR and Cu O-6MR-2 species only differ in the arrangement of the 2Al position on the 6-MR which alters the local electronic density of the Cu^{2+} ions within the 6MR site (Figure 3d).[34] We have approved that $[Cu–O–Cu]^{2+}$ species were not present for the samples activated at 500 °C for 12 h under vacuum. Both Cu^{2+} and $[Cu(OH)]^+$ ions in Cu-containing SSZ-13 are active for the NH_3-SCR-DeNO$_x$. Paolucci et al.[6] demonstrated similar activation and reaction energies for the two active sites. Furthermore, Tronconi et al.,[36,37] as well as Daya et al.,[15] indicated that there is no need to differentiate between Cu^{2+} and $[Cu(OH)]^+$ in describing reduction half-cycle (RHC) kinetics. Contrary, Liu et al.[38] claimed that $[Cu^{II}(NH_3)_3(OH)]^+$ is more reactive than $[Cu^{II}(NH_3)_4]^{2+}$ and that the NO reduction of $[Cu^{II}(NH_3)_3(OH)]^+$ is kinetically significant in the initial stage of the low-temperature RHC pathway.

3.3. Catalytic and Spectroscopic Studies

We conducted our catalytic experiments, including temperature-programmed studies, without water vapor in the feed to prevent the competitive adsorption between NH_3 and H_2O on the active sites. Figure 4a-c presents NO conversion and selectivity during standard NH_3-SCR-DeNO$_x$ ($4\ NO + 4\ NH_3 + O_2 \rightarrow 4\ N_2 + 6\ H_2O$). Cu-SSZ-13_MFI_5, Cu-SSZ-13_BEA_6, and Cu-SSZ-13_FAU_7 can operate in the temperature window of 150-500 °C, which is required for its application in exhaust systems.

The NO conversion results reported for these catalysts are similar to the other Cu-containing SSZ-13 given in our last publications.[13,16] The correlation of the Cu loading together with NO conversion at 150 °C (Figure S9) revealed that the Cu-SSZ-13_MFI_4 sample exhibits the lowest NO conversion among all samples (below 400 °C), which is attributed to its lower copper content. An exception from this correlation is Cu-SSZ-13_FAU_7 (with 4.72 wt.% of Cu), which exhibited a similar conversion to both Cu-SSZ-13_MFI_5 and Cu-SSZ-13_BEA_6 (with 3.41–3.59 wt.-% of Cu). The three catalysts with the highest NO conversion possess the highest copper loading and the lowest particle sizes. However, the nature of the introduced species is closely related to the n(Si)/n(Al) ratio of the sample. Thus, Cu-SSZ-13_FAU_7, with a n(Si)/n(Al) ratio of 16.70 was overexchanged with copper species, which led to the formation of Cu_xO_y species in the catalyst. Consequently, this sample along with Cu-SSZ-13_MFI-5 and Cu-SSZ-13_BEA_6, exhibited one of the highest activity for NH_3 oxidation. Above 300 °C, NO conversion reflects the NH_3 oxidation ability of the respective catalysts, as the oxidation of ammonia is a competitive side reaction of NH_3-SCR-DeNO$_x$.

Prodinger et al.[39] focused on the effect of the particle size of the Cu-SSZ-13 (yielding particle sizes ranging between 260 nm and 1.3 µm, while the n(Si)/n(Al) ratio was maintained constant, thus keeping similar Al and Cu content, in NH_3-SCR-DeNO$_x$. However, they reported comparable catalytic properties and hydrothermal stability for the Cu-containing SSZ-13 samples independent of their particle size. Thus, they claim that intracrystalline mass transfer limitations are not significant under the applied conditions. This is further approved in our NH_3-SCR-DeNO$_x$ experiments with different grain sizes. We tested the catalytic activity of Cu-SSZ-13_MFI_1 and Cu-SSZ-13_MFI_5 in

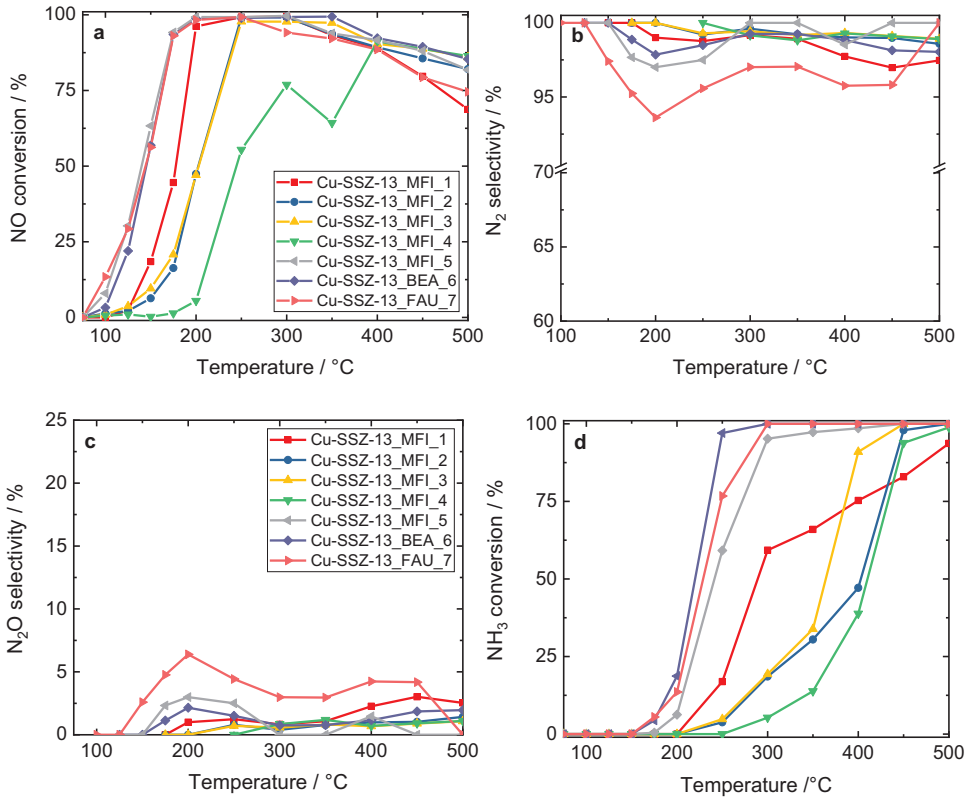

Figure 4. NO conversion a) and selectivity b-c) of Cu-containing SSZ-13 samples during NH_3-SCR-DeNO$_x$. Reaction conditions: m_{cat} = 0.1 g, c(NO) = 0.1 vol.%, c(NH_3) = 0.1 vol.%, c(O_2) = 10 vol.%, diluted in He, F_{TOT} = 120 mL min^{-1}, GHSV = 30,000 h^{-1}, and d) NH_3 oxidation. Reaction conditions: m_{cat} = 0.1 g, c(NH_3) = 0.1 vol.%, c(O_2) = 10 vol.%, He balance, F_{TOT} = 120 mL min^{-1}, GHSV = 30,000 h^{-1}.

three different ranges of grains (100–200 µm, 200–400 µm, and 400–500 µm). For these two samples, no difference in activity was found in the studied temperatures, i.e., below 150 °C.

All the materials were N_2 selective, presenting more than 95% N_2 selectivity up to 500 °C (Figure 4b). For all the samples, a small amount of N_2O was also detected above 300 °C as a result of NH_3 oxidation. Only for Cu-SSZ-13_FAU_7, N_2O was detected below 200 °C due to NH_4NO_3 formation, and above 200 °C due to NH_3 oxidation.[40] Our last data for Cu-SSZ-13 based on FAU zeolite revealed N_2O formation below 55 ppm for the whole studied temperature range.[22] Apparently, the formation of N_2O is favored over amorphous Cu_xO_y species. Still, lower N_2O is found over Cu-SSZ-13_FAU_7 than over Cu-containing Y-zeolites (e.g.,[41,42]). According to the mechanism proposed by Feng et al.,[43] the selectivity towards N_2O is influenced by the availability of Brønsted acid sites. Catalysts with a high Cu loading lack sufficient Brønsted acid sites for the decomposition of H_2NNO and HONO intermediates in the NH_3-SCR-DeNO$_x$ cycle, leading to a higher expected selectivity towards N_2O, which can also be applied to our case. Contrary to that, our last studies over commercial SSZ-13 samples did not reveal any N_2O formation.[16]

Cu_xO_y species on the external surface of the zeolites were responsible for the oxidation of NH_3 into NO_x (Figure 4d), while Cu^{2+} species in zeolite cages are responsible for the reduction of NO_x into N_2 following the i-SCR reaction mechanism. However, according to Wang et al.,[44] NH_3-solvated mobile $[Cu^{II}(NH_3)_3OH]^+$ species are active for the NH_3 oxidation at low temperatures, and the same species further catalyze the reduction of NO (produced from NH_3 oxidation) to N_2 and H_2O.

Based on the outcome of NH_3-SCR-DeNO$_x$, we selected three samples, i.e., Cu-SSZ-13_MFI_2, Cu-SSZ-13_MFI_5, and Cu-SSZ-13_BEA_6, for a further investigation of the reaction intermediates to discriminate the contribution of quantity and reactivity change in the active sites in the Cu-containing SSZ-13. In particular, Cu-SSZ-13_MFI_2 has a much lower Cu content and particle size that is more than five times larger than that of the other samples. Meanwhile, Cu-SSZ-13_MFI_5 and Cu-SSZ-13_BEA_6, with very similar compositions and catalytic performances, were selected to approve the mechanistic insight.

Figure 5a,b show in situ DRIFTS spectra of the Cu-SSZ-13_MFI_5 and Cu-SSZ-13_BEA_6 samples after their exposure to 0.1 vol.% NH_3 diluted in N_2 for 0.5 h followed by an exposure to 0.1 vol.% NO. Two distinct peaks can be singled out from the graph. The first one at around 1457 cm^{-1} is related to the bending vibration of NH_4^+ cations on Brønsted acid sites (B-NH_4^+), while the second one at around 1269 cm^{-1} is related to the vibration of the N-H bond from adsorbed ammonia on Cu sites (attributed to the Lewis acid sites, L-NH_3, Cu-NH_3).[45,46] For Cu-SSZ-13_MFI_5 and Cu-SSZ-13_BEA_6 with pre-adsorbed NH_3, the peak related to NH_4^+ cations increased after their exposure to NO, indicating the reaction of Cu^{2+} sites to Cu^+ with the formation of H^+ intermediates. Furthermore, the reaction between H^+ intermediates and NH_3 leads to NH_4^+ cations.[6,47] The reduction of Cu^{2+} sites

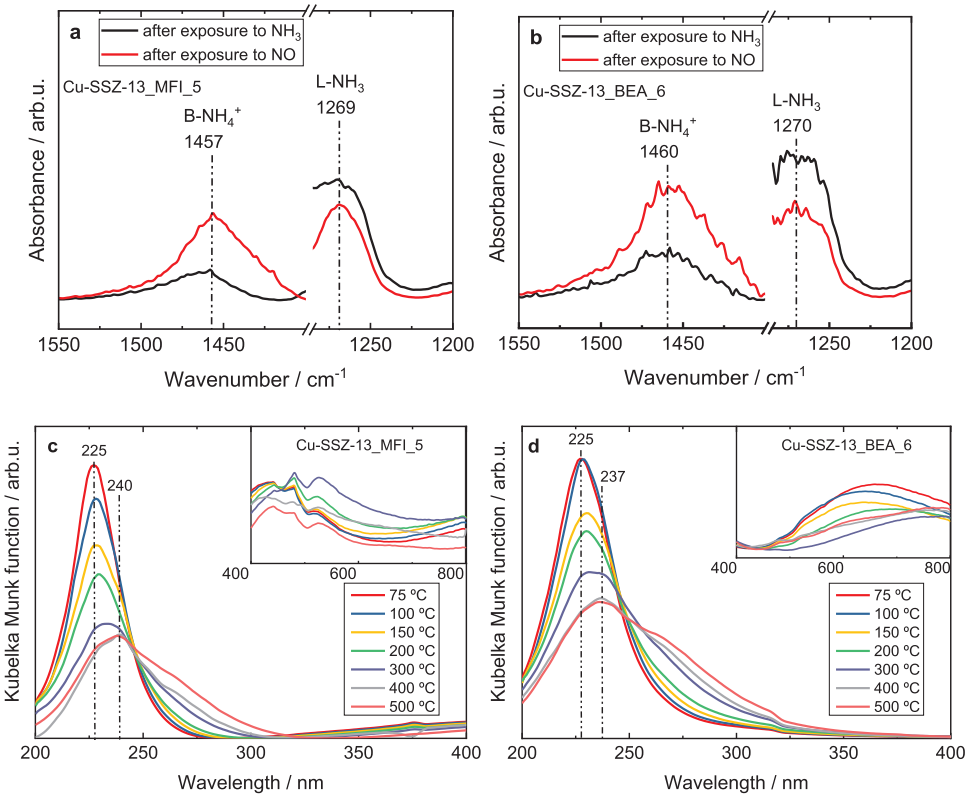

Figure 5. DRIFTS spectra recorded at 150 °C of a) Cu-SSZ-13_MFI_5 and b) Cu-SSZ-13_BEA_6 after exposure to NH_3 and a subsequent exposure to NO. Reaction conditions: $c(NH_3)$ = 0.01 vol.%, $c(NO)$ = 0.01 vol.%, diluted in N_2, as well as in situ DR UV–vis spectra of c) Cu-SSZ-13_MFI_5 and d) Cu-SSZ-13_BEA_6 during NH_3-SCR-DeNO$_x$ at a range of temperatures. Reaction conditions: $c(NH_3)$ = 0.045 vol.%, $c(NO)$ = 0.045 vol.%, $c(O_2)$ = 10 vol.%, diluted in N_2.

is also indicated by the decrease in intensity of the second peak after exposure to NO. Similar results were obtained over other samples, such as Cu-SSZ-13_MFI_2 and Cu-SSZ-13_MFI_3 (Figure S10), as well as in previously reported SSZ-13-based samples.[16] Nevertheless, the intensity of the respective lines varied depending on the available copper species, in line with the ICP-OES data and the differences in catalytic activity of these materials. NH_4^+ intermediates near Cu^+ sites are expected to interact with nitrosamines (H_2NNO), resulting in the formation of N_2 and H_2O.[48] H_2NNO forms as a reaction product between NH_3 and NO^+ (activated via the cage-confined $[Cu^I(NH_3)_2]^+$ pairs). Furthermore, the cation conductivity of Cu-SSZ-13_MFI_5 and Cu-SSZ-13_BEA_6 was investigated by in situ impedance spectroscopy coupled with in situ DRIFTS. In Figure S11, the normalized signal of the ionic conductivity, as well as the normalized IR signal related to NH_4^+ cations on Brønsted acid sites (ca. 1457 cm^{-1}) can be observed. During the ammonia adsorption step, both samples experience an increase in ionic conductivity, while the IR band related to B-NH_4^+ steadily rises. However, as NH_3 is cut off and NO is introduced, a significant increase in the B-NH_4^+ signal can be observed as described before. Nevertheless, for both catalysts, the sudden increase in ionic conductivity decreases in time, possibly due to the consumption of ammonia on Cu sites (Figure S11c,e) upon exposure to NO, which occurs to a greater extent than upon exposure to N_2 (Figure S11d,f) and can be observed through the evolution of the band ca. 1290 cm^{-1}. This might indicate that, for these catalysts, both NH_4^+ ions and Cu-bound ammonia species contribute significantly to the ionic conductivity of the zeolite.

Figure 5c,d shows in situ DR UV–vis spectra during NH_3-SCR-DeNO$_x$ over Cu-SSZ-13_MFI_5 and Cu-SSZ-13_BEA_6. Below 200 °C, NH_3 solvates over Cu^+ species forming linear $[Cu^I(NH_3)_2]^+$ reaction intermediates. Two of these linear intermediates can diffuse 0.9 nm away from their ionic site towards each other and, in the presence of O_2, react to form $[(NH_3)_4Cu^{II}{}_2O_2]^{2+}$.[12,17] In our previous works, we have attributed the formation of the μ-η^2,η^2-peroxo diamino dicopper (II) complex ($[(NH_3)_4Cu^{II}{}_2O_2]^{2+}$) to a broad band in the d-d region centered at ca. 720 nm, along with a red-shift of the ligand-metal charge transfer (LMCT) transitions (e.g.,[13,14]). Furthermore, the $[(NH_3)_4Cu^{II}{}_2O_2]^{2+}$ complex can be identified by in situ DR UV–vis by a distinct absorption at 350 nm and is consistent with an absorption band at 225 nm.[48,49] Upon exposure of both Cu-SSZ-13_MFI_5 and Cu-SSZ-13_BEA_6 to an NH_3-SCR-DeNO$_x$ feed at 75 °C, a distinct band at around 225 nm becomes prominent. The band related to this compound reaches its highest intensity at the lowest temperature, but as the temperature increases, it diminishes above 200 °C. The disappearance of this band is due to the loss of the NH_3 solvation shell of copper species; thus, the mobility of the Cu diminishes. Other bands with a maximum at 660 nm were more pronounced for Cu-SSZ-13_BEA_6. The band located at 350 nm is not visible for both samples. The absence of the band

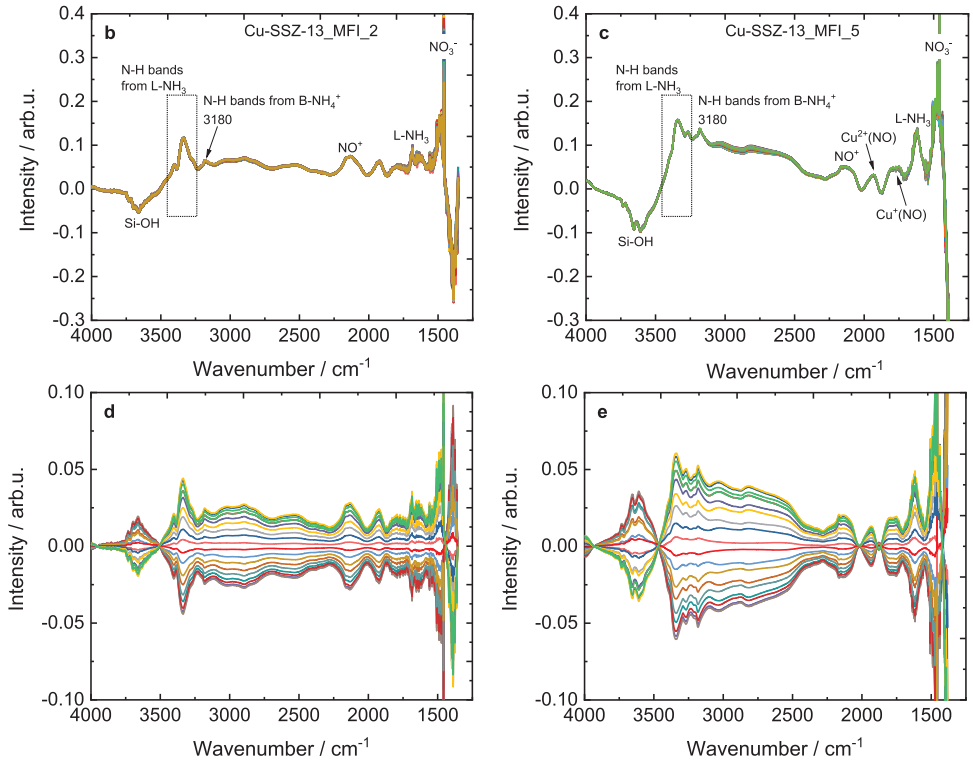

Figure 6. Schematic description of the concentration pulse sequence used for the modulated excitation experiments, and in situ IR spectra on b) Cu-SSZ-13_MFI_2 and c) Cu-SZ-13_MFI_5 and d, e) corresponding phase-resolved spectra. Reaction conditions: $c(NH_3)$ = 0.1 vol.%, $c(NO)$ = 0.1 vol.%, $c(O_2)$ = 10 vol.%, diluted in Ar.

at 350 nm suggests that the amounts of Cu dimers is very low in both samples. Similarly, in our previous studies, we reported the differences in the intensity of this band for Cu-containing SSZ-13 with different $n(Si)/n(Al)$ ratios,[16] hence, with different copper content.

Figures 6b,c and S12 present the IR spectra recorded during transient experiments as indicated in Figure 6a. Thus, in the first approach, NH_3 and O_2 were introduced to the catalysts for adsorption over Cu-SSZ-13_MFI_2 and Cu-SSZ-13_MFI_5 at 125 °C (Figure 6a,b). The peaks associated with NH_3 coordinated to Lewis acid sites (L-NH_3) appeared at ca. 1623–1627 cm^{-1}, together with the strong peaks at 3500–3250 cm^{-1} assigned to the stretching modes of N-H vibrations of L-NH_3. The negative peaks in the range of 3445–3925 cm^{-1} appeared due to both external and internal silanols groups (Si—OH), as a result of NH_3 adsorption on Lewis acid sites reactions.[50] The Cu-SSZ-13_MFI_5 material possesses a higher NH_3 sorption capacity than Cu-SSZ-13_MFI_2, which is reflected by the higher intensity of the FT-IR spectra (as well as NH_3-TPD, Figures S17a and S19a). As the solvation of NH_3 into the Cu coordination sphere is the first step of the SCR reaction, $[Cu^{II}(NH_3)_4]^{2+}$ and $[Cu^{II}(OH)(NH_3)_3]^{+}$ are assumed to be formed. In the next step, a gas mixture of NO and O_2 was introduced, which resulted in the reduction of Lewis acid sites. This can be supported by the increased intensity of the positive peak at ca. 3657 $cm^{-1,}$ indicative of adsorbed H_2O. After switching back to the mixture of NH_3 and O_2, the Lewis acid sites were partly restored. After running the NH_3-SCR-DeNO$_x$ for 30 min, a repeatedly pulsing of NO followed (Figure 6a). After phase-sensitive detection (PSD, Figure 6d,e) transfer, both Cu-SSZ-13_MFI_2 and Cu-SSZ-13_MFI_5 responded to the NO pulsing in the range of 3800–2700 cm^{-1} and 2300–1250 cm^{-1}. NH_3 first filled the copper coordination sphere, followed by Brønstead acid sites, while both of the sites responded to the NO modulated excitation (ME) experiments. The surface of both catalysts is dominated by the Cu^{+}(NO) mononitrosyls (1930 cm^{-1}), Cu^{+}(NO) species (1775 cm^{-1}), and peaks related to NO^{+} and NO_3^{-} species appeared at ca. 2130 cm^{-1} and 1460 cm^{-1}, respectively.[13] Again taking into account the solvation with NH_3 as the first step of the NH_3-SCR-DeNO$_x$ process, these bands can be assigned to ammino-complexes, as approved by in situ IR and DFT calculations.[9,19]

3.4. Transient and Temperature-Programmed Studies

Figures S13 and S14 show the normalized concentration of the main compounds ($^{15}NH_3$, $^{14}NH_3$, $^{14}N_2$, $^{14}N^{15}N$, $^{15}N_2$, Kr, and Ar) during the SSITKA experiments over Cu-SSZ-13_MFI_5 and Cu-SSZ-13_BEA_6, at 100 °C (NO conversion below 25%), 125 °C (NO conversion below 50%), and 150 °C (NO conversion below 75%). For comparative purposes, we also included results for Cu-SSZ-13_MFI_2 (Figure S15). The delay between the decrease of $^{14}NH_3$ and the Ar signal, as well as the delay between the increase of $^{15}NH_3$ and Kr, proves that ammonia is reversibly adsorbed on the surface of the catalysts. On the other hand, the large delay between $^{14}N_2$ and Ar suggests that the reaction intermediates

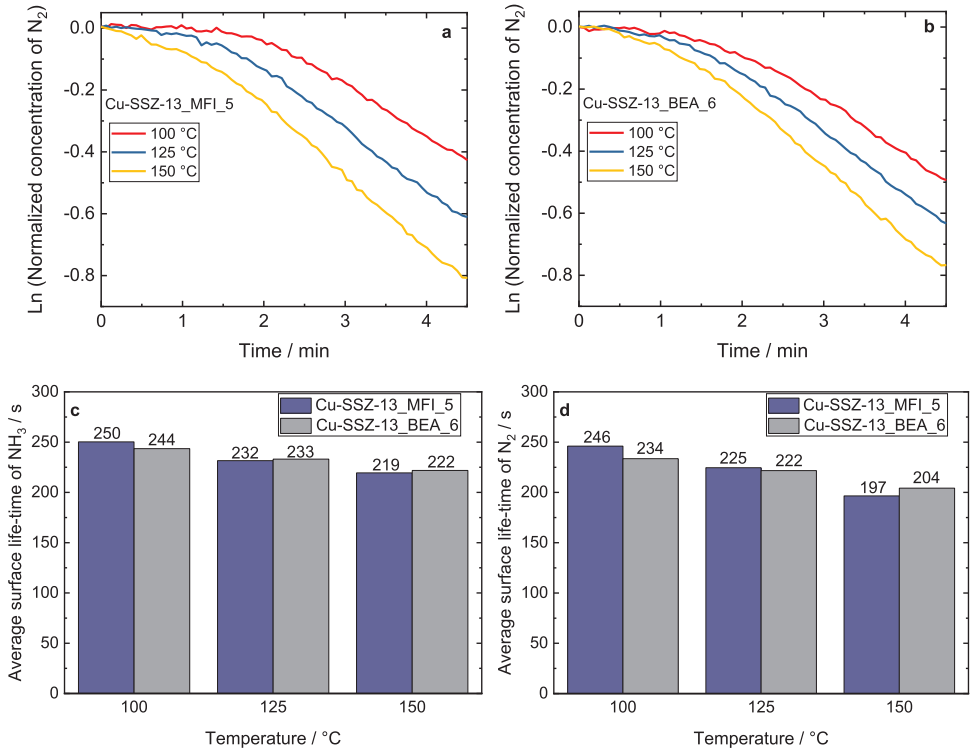

Figure 7. Logarithm of the normalized response of $^{14}N_2$ after the isotope switch during the SSITKA experiments over a) Cu-SSZ-13_MFI_5 and b) Cu-SSZ-13_BEA_6, average surface life-time of absorbed c) NH_3 and d) N_2.

are present on the catalyst surface for a long time. Moreover, the minor contribution of $^{15}N_2$ in the reactor output compared to $^{14}N^{15}N$ proves that nitrogen is mainly formed by one nitrogen atom of nitrogen oxide and one nitrogen atom of ammonia. Nonetheless, the presence of $^{15}N_2$ suggests that other processes occur in addition to NH_3-SCR-DeNO$_x$. The only pathway in which $^{15}N_2$ could be formed is through ammonia oxidation (NH_3-SCO). No other products with labeled nitrogen can be detected, which is in line with the selectivity values at that range of temperatures for the Cu-SSZ-13_MFI_5 and Cu-SSZ-13_BEA_6 catalysts.

Figures 7a,b and S16a show the logarithm of the normalized response of $^{14}N_2$ after the isotope switch for both materials. The response of this value over time can be used to fit a mechanistic model for the catalysts. The surface of the catalyst can be regarded as a group of interconnected pools, which are considered as homogeneous systems within the reaction pathway and, in each pool, a reaction intermediate can be formed, adsorbed and desorbed. This model does not conceive hold-up times between pools, except for the residence time of a reaction intermediate in a pool.[51] The mechanistic model that fits the logarithm of the normalized response of $^{14}N_2$ for both catalysts is the pools in the series model, where the exit of a pool is connected to the entrance of the next, and the surface life-time can be calculated as the sum of the surface life-time of each pool.[52] However, this interpretation considers that the only reaction that takes place is the NH_3-SCR-DeNO$_x$. With some caution, it can be suggested that both processes (NH_3-SCR-DeNO$_x$ and NH_3-SCO) proceed according to a pools-in-series model.

Figure 7c,d presents the average surface life-time of NH_3 and N_2 on Cu-SSZ-13_MFI_5 and Cu-SSZ-13_BEA_6 (Figure S16b,c for Cu-SSZ-13_MFI_2). With the increase in temperature, a significant decrease in the average surface life-time of both NH_3 and N_2 was observed, indicating that the reactants and products stay for a shorter time on the surface of the catalysts due to the increase in the reaction rate. The calculation of the surface concentration of NH_3 and N_2 was not as straightforward as in our previous study[16] due to the coexistence of both NH_3-SCR-DeNO$_x$ and NH_3-SCO already below 150 °C, which was not previously detected. As both reactions occur simultaneously, the assessment of which NH_3 and N_2 molecules are consumed and formed by each reaction is beyond our current means.

Figure S17a,b show the desorption of NH_3 in pure helium or in the mixture of O_2/He, respectively over Cu-SSZ-13_MFI_5. In the temperature-programmed desorption studies of NH_3 in He, two main peaks can be observed between 210 °C and 350 °C, indicating the presence of adsorbed NH_3 on Lewis acid sites (Cu^{2+} isolated sites), and on Brønsted acid sites,[53,54] respectively. It is worth mentioning that some studies assigned these two respective peaks of NH_3 desorption in Cu-SSZ-13 from six- (6MRs) and eight-membered rings (8MRs), respectively.[55,56] In the profile recorded for the desorption of NH_3 in the presence of O_2/He mixture (Figure S17b), there was a significant contribution to H_2O, indicating that a selective catalytic oxidation of ammonia into N_2 and H_2O occurs. Indeed, Cu-SSZ-13_MFI_5 possesses aggregated Cu_xO_y species (Figures 3b and 4d) that are active species for NH_3 oxidation. Further experiments approved NH_3 as the main adsorbed species, while NO was adsorbed

on the surface of this catalyst only to a minor degree. NH_3 oxidation is preferred in other experiments where NH_3 is pre-adsorbed while O_2 is dosed from the gas phase (Figure S17g). The desorption of NO_2 indicates (Figure S17d) that NO is partly oxidized by O_2 on the surface of the catalyst. Otherwise, the reaction between adsorbed NH_3 and NO from the gas phase led to the formation of N_2 and H_2O (Figure S17e) up to 400 °C. Above 400 °C, the signals of NH_3, N_2 and H_2O recede, while the NH_3 oxidation starts to be more prominent than the NH_3-SCR-DeNO$_x$.

Figure S18 presents the selected experiments performed for Cu-SSZ-13_BEA_6. Due to their similar physico-chemical characteristics, such as particle size and copper content, the TPD results are comparable to the ones seen above for Cu-SSZ-13_MFI_5. Figure S19 depicts the temperature-programmed desorption experiments performed over Cu-SSZ-13_MFI_2. Notably, this catalyst exhibits a reduced desorption of ammonia at 350 °C compared to the other two catalysts (Figure S19a). Moreover, the desorption of NH_3 in the presence of O_2/He indicates that the NH_3 oxidation takes place, although to a minor degree as compared to the other two catalysts. Cu-SSZ-13_MFI_2 has also exhibited diminished NO adsorption capabilities (Figure S19c), which contributes to its lower N_2 production during the desorption of NO + O_2 under an NH_3 flow (Figure S19d). The reaction of adsorbed NH_3 with NO and O_2 (from the gas phase) results in N_2 formation up to 450 °C, potentially due to the reduced NH_3 oxidation activity of this sample relative to the other two (Figure 4d). Furthermore, the desorption of NO and O_2 under the flow of the $^{15}NH_3$ isotope (complementary to the experiment with non-labeled NH_3) was also performed (Figure 8c–e versus Figures S17d, S18b, and S19d). The $^{14}N^{15}N$ formation indicates that it is formed from NH_3 and NO during NH_3-SCR-DeNO$_x$. Interestingly, a peak of *m/z* 30 at the same temperature can also be seen. This approved that $^{15}N_2$ is formed as a result of the selective catalytic oxidation of ammonia over the catalysts, which occurs simultaneously as NH_3-SCR-DeNO$_x$. This is also approved by the presence of a *m/z* 30 signal above 200 °C during the desorption of $^{15}NH_3$ over NO and O_2 (Figure S17f). Also, Fedyna et al.[8] showed that above 200 °C, the NH_3-SCR-DeNO$_x$ is accompanied by NH_3 oxidation. Furthermore, they claimed that ammonia may be released from the coordination sphere of the Cu^{2+} sites, migrating to the chabazite cage and reacting through the NH_3 oxidation (at ca. 300 °C), mainly due to the strong NH_3-SCR-DeNO$_x$ domination, which results in an excess of NH_3 molecules. Overall, N_2 is mainly formed as a product of the reduction of pre-adsorbed NH_3 and NO (dosed from the gas phase), which is in line with our previous studies.[16] Besides, NH_3 oxidation leads to N_2 formation between 150–450 °C, as well as reduction of in situ formed NO_x^- species via NH_3 from the gas phase. Comparing these results with the N_2 production over Cu-SSZ-13_BEA_6, there is a small shift towards lower temperatures of the N_2 generated from the NH_3 oxidation. However, the N_2 signal from the desorption of NO and O_2 over a flow of NH_3 shows the same results.

3.5. DFT Modelling Results

Density functional theory (DFT) was used to evaluate the possible reaction pathways in the NH_3-SCR-DeNO$_x$ reaction (details in the Supporting Information). Leaning on the experimental observations in this work and existing literature data (e.g.,[9,19]), we propose the following pathway. In the oxidation half-cycle, a pair of $(NH_3)_2Cu^I$ complexes activates an O_2 molecule to produce the μ-η^2,η^2-peroxo diamino dicopper(II)-complex intermediate (Figure 9, structure **2**), as observed by in situ DR UV–vis spectra measurements (Figure 5c,d). This intermediate is well reported in the literature, with some controversy regarding its stability relative to the trans-μ-1,2-peroxo diamino dicopper(II) intermediate, shown as structure **12**.[17,55] Different computational approaches exhibit conflicting data on the relative stabilities of the two intermediates.[56] In this work, we adopted a Hubbard correction approach, which predicts the intermediate **2** to be energetically favored (for 0.03 eV) compared to **12**, consistent with recent findings.[55,56] Due to a small energy difference, our calculations suggest that both intermediates can form. We tested several values of the Hubbard *U* (0, 2, 4 and 6 eV) and noted that the minimum *U* value which produces the correct order of relative stabilities is 6 eV. Further discussion on the methodology is given in the section Importance of the Hubbard correction in the Supporting Information. With the introduction of NO in the system, the cycle progresses by the attachment of NO and NH_3, and a transfer of one H atom from NH_3 to O (intermediates **3** and **4**), followed by the detachment of H_2NNO and subsequent decomposition into N_2 and H_2O.

The reduction half-cycle has been proposed to follow multiple pathways. It can proceed by several steps in which H_2NNO is produced (**5** through **9**). We note that the reaction intermediates and their energies are in good agreement with previous theoretical work.[7] Moreover, the experimental evidence supporting the structure **9** recently obtained by Tarach et al.,[9] and indicated in this work by IR measurements (Figure 6), further supports this structure and the presence of the related reduction half-cycle in this work. Another pathway through which the copper reduction can proceed is by the creation of HONO intermediates (**10, 11**).[10,57]

Interestingly, the intermediate **10** is similar to a *two-p* structure obtained in[10] - a proximal configuration of two $[Cu^{II}(OH)(NH3)_3]^+$ species - while our calculations suggest dimerization. The bond lengths between copper atoms and bridging oxygen atoms are not the same length, implying a structure between two proximal species and a fully symmetrical dimer. This structure follows naturally from **7**, thus connecting it to the OHC characterized by the μ-η^2,η^2-peroxo diamino dicopper(II)-complex intermediate detected by in situ DR UV–vis measurements. Therefore, the intermediates do not have to split into two species prior to the HONO pathway, and the split could instead be a consequence of the reactions with NO, similar to in the H_2NNO pathway. The intermediate **10** can, in principle, be viewed as an intermediate **7** solvated by more amino species, a simi-

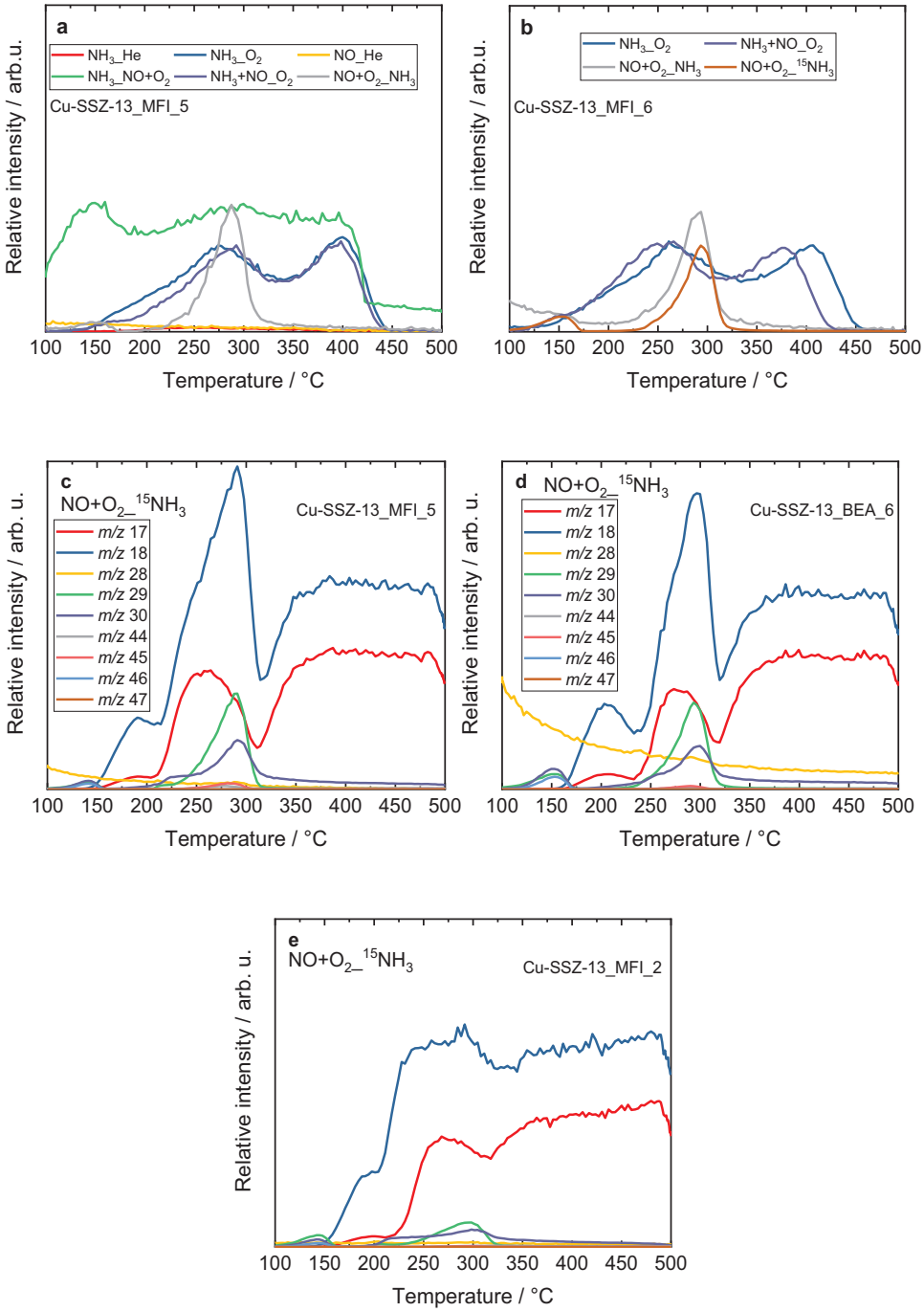

Figure 8. Formation of N_2 during temperature-programmed desorption over a) Cu-SSZ-13_MFI_5, and b) Cu-SSZ-13_BEA_6. The mass-to-charge of *m/z* 29 is used for the detection of $^{15}N^{14}N$. Temperature-programmed desorption of NO + O_2 in $^{15}NH_3$ over c) Cu-SSZ-13_MFI_5, d) Cu-SSZ-13_BEA_6, and e) Cu-SSZ-13_MFI_2.

larity reflected in their nearly identical energies. As such, they might coexist in an equilibrium, in proportion depending on the temperature and concentration of NH_3 in the system. The relative energies of the following intermediates in both cycles are also rather similar (**8, 9,** and **11**), which is consistent with a recent report that pathways can be present simultaneously.[16]

Finally, a pathway that involves copper(II) nitrates is considered, as some related species were detected in this work by IR measurements. This pathway is tentatively connected to the others via intermediate **12**, which is supported by previous computational work,[58] although the initial steps to **13** and **14** might also involve copper detachment from the zeolite framework. We note that, although a much different DFT approach was used, the complex **14** is consistent with the structure suggested by experiments and calculations by the work of Negri et al.[19] Although the relative energies of the intermediates in this pathway compare favorably with the first few intermediates in the other cycle (**13** is 2.2 eV lower in energy than **3**),

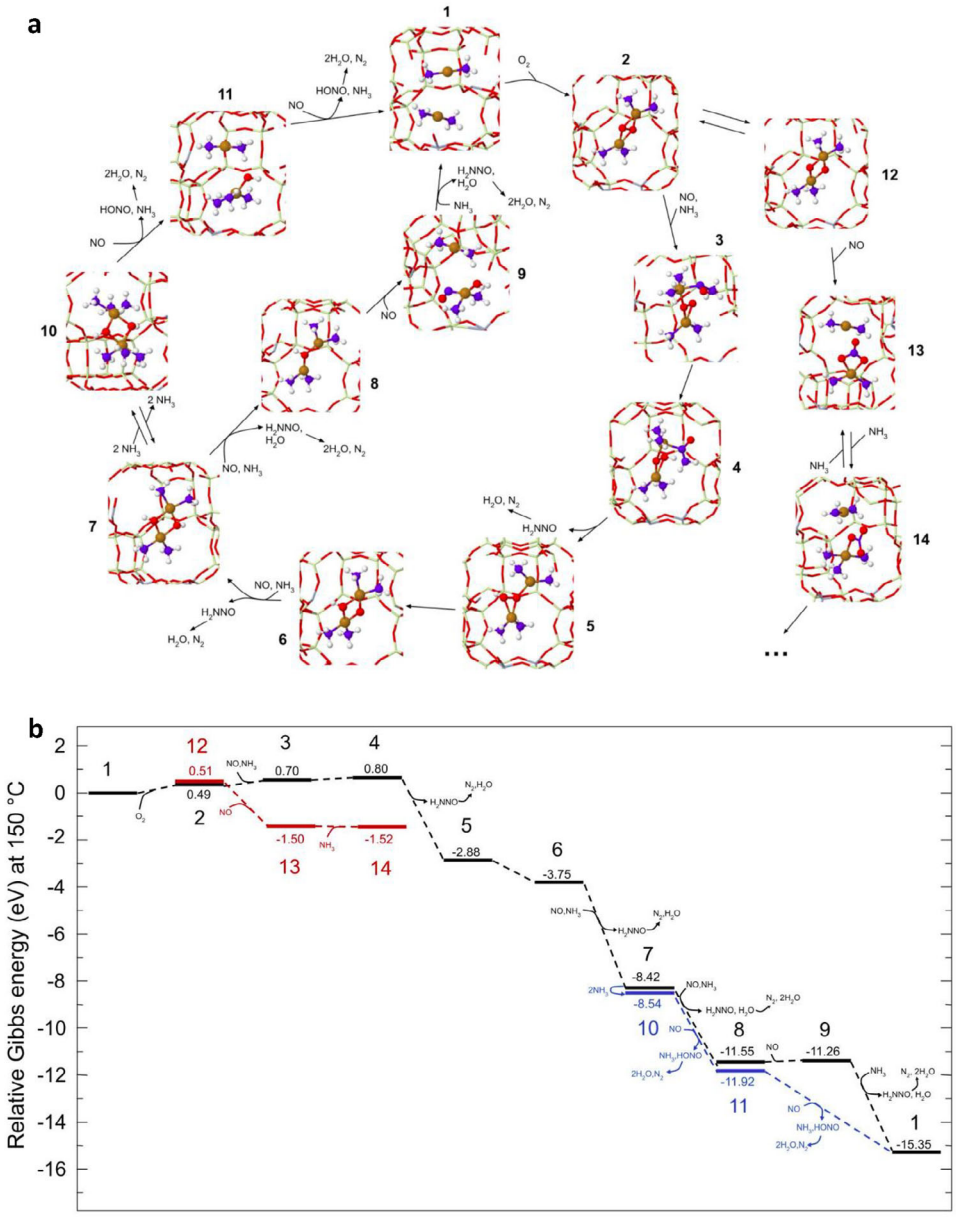

Figure 9. a) Proposed pathways of the NH_3-SCR-DeNO$_x$ reaction connecting the most probable intermediates (based on experimental observations and computations). Reaction intermediates are shown as ball-and-stick models while the CHA cage is shown as a wireframe. For better clarity and visibility of the intermediates, a part of the CHA cage is removed. Oxygen atoms are colored red, nitrogen blue, hydrogen white, copper brown, silicon light yellow, and aluminum grey; b) Relative Gibbs energies of the stable intermediates with colors depicting different pathways or branches of the cycle.

which explains the indications of their presence by experimental results, the rest of this pathway is considered to be relevant only at much higher temperatures. This is evidenced by reports of high calculated activation energies in the proposed reaction steps following these intermediates.[58] For that reason, and since proposing the alternative is not within the scope of this work, the pathway is modelled only until the intermediate **14**.

Overall, the DFT results provide a comprehensive reaction framework consisting of multiple branches. These branches are constructed around intermediates consistent with experimental findings, thus supporting the thermodynamic feasibility of their presence in the catalytic cycle and contextualizing them within the proposed reaction pathway.

4. Conclusions

A series of Cu-containing samples of zeolite SSZ-13 (Cu-SSZ-13) with structure topology CHA were prepared from zeolites with different structure topologies (MFI, BEA, FAU) and were tested in NH_3-SCR-DeNO$_x$. These studies provide a systematic application and comparison of interzeolite conversion using various parent zeolite materials under customized synthesis conditions, providing new insights into how the choice of precursor influences the properties of the final catalyst. Although the Cu-SSZ-13 obtained from different zeolite structure topologies revealed similar catalytic activity, significantly higher N_2 selectivity was reached over materials obtained from MFI and BEA topologies.

The activity and N_2 selectivity of the catalysts were recognized to be influenced by their particle size, and the nature and location of Cu species, which in turn were affected by the *n*(Si)/*n*(Al) ratio of these materials. The detailed reaction mechanism is still under debate, indicating the complexity of both RHC and OHC. The spectroscopic, temperature programmed (including studies with isotopes) as well as transient studies revealed the intermediates of reduction and oxidation half-cycles, including NH_4^+, NH_x^-, $[(NH_3)_4Cu^{II}{}_2O_2]^{2+}$, NO_2^-/NO_3^- species. Thus, we approved the significance of nitrites/nitrates as intermediates in NH_3-SCR-DeNO$_x$. Furthermore, the DFT modelling confirmed that the presence of the mentioned intermediates is thermodynamically possible. NH_3-SCR-DeNO$_x$ predominantly involves the reaction between NH_3 adsorbed on the catalyst surface and NO (dosed from the gas phase), however, the reaction between adsorbed NO_x^- species (nitrites/nitrates) and NH_3 also takes place. Above 200 °C, both the NH_3-SCR-DeNO$_x$ and NH_3 oxidation occur, which is approved by applying isotopically labeled NH_3. The investigations provide a pathway to gain deeper insights into the relationships between the structure and activity of zeolite-based materials.

Author Contributions

A.M.R: Conceptualization; methodology; investigation; data curation; writing—original draft; software; data management. **A.P**: Investigation; writing—review & editing. **M.B**: Modelling; software; writing—DFT modelling part. **J.Y**.: Investigation; data curation. **M.R**: Investigation; data curation; writing—review & editing. **M.F.L**.: Investigation; data curation; writing—review & editing. **Anqi Guo**: Investigation; data curation. **M.B**.: Investigation; data curation. **M.H**.: Modelling; software; writing – DFT modelling part. **J.Z**.: Review. **U.S**.: Review. **A.P**. Review. **N.T**.: Writing—review & editing. **M.J**.: Conceptualization; methodology; investigation; data curation; writing—original draft; writing—review & editing; supervision; data management; project management; visualization; resources.

Acknowledgments

M.J. acknowledges a DFG Research Grant JA 2998/2–1. A.P. acknowledges the Croatian Science Foundation for funding, project ID: UIP-2019–04–4977 and Deutscher Akademischer Austauschdienst project Research Stays for University Academics and Scientists, project ID: 202457693448. M.F.L. acknowledges a DFG Research Grant of GRK:2721 and thanks Dr. Winfried Böhlmann for the technical assistance on the dehydration procedure. M.J. and M.R. acknowledge NAWA-DAAD Nr. BPN/BDE/2023/1/00001/U/00001. N. N. T. acknowledges the Slovenian Research and Innovation Agency for funding through research programs P1-0418, P2-0152 and project N2-0291.

Open access funding enabled and organized by Projekt DEAL.

Conflict of Interests

The authors declare no conflict of interest.

Data Availability Statement

The data that support the findings of this study are available in the supplementary material of this article.

Keywords: Copper species · Intermediates · Interzeolite conversion process · NH_3-SCR-DeNO$_x$ · Reduction and oxidation cycles · SSZ-13

[1] *Zeolites in Catalysis*, (Eds: J. Cejka, R.E. Morris, P. Nachtigall), Royal Society of Chemistry, Cambridge **2017**.
[2] J. Wang, H. Zhao, G. Haller, Y. Li, *Appl. Catal. B: Environ.* **2017**, *202*, 346–354.
[3] M. Jabłońska, M. E. Potter, A. M. Beale, *ChemCatChem* **2024**, *16*, e202301214.
[4] J.a Hun Kwak, H. Zhu, J. H. Lee, C. H. F. Peden, J. Szanyi, *Chem. Commun.* **2012**, *48*, 4758–4760.
[5] C. Negri, M. Signorile, N. G. Porcaro, E. Borfecchia, G. Berlier, T. V. W. Janssens, S. Bordiga, *Appl. Catal. A: Gen.* **2019**, *578*, 1–9.
[6] C. Paolucci, A. A. Parekh, I. Khurana, J. R. Di Iorio, H. Li, J. D. Albarracin Caballero, A. J. Shih, T. Anggara, W. N. Delgass, J. T. Miller, F. H. Ribeiro, R. Gounder, W. F. Schneider, *JACS* **2016**, *138*, 6028–6048.
[7] L. Chen, T. V. W. Janssens, P. N. R. Vennestrøm, J. Jansson, M. Skoglundh, H. Grönbeck, *ACS Catal.* **2020**, *10*, 5646–5656.
[8] M. Fedyna, B. Mozgawa, F. Zasada, K. Góra-Marek, J. Gryboś, W. Piskorz, C. Yin, Z. Zhao, P. Pietrzyk, Z. Sojka, *Appl. Catal. B: Environ.* **2023**, *325*, 122309.
[9] K. A. Tarach, M. Jabłońska, K. Pyra, M. Liebau, B. Reiprich, R. Gläser, K. Góra-Marek, *Appl. Catal. B: Environ.* **2021**, *284*, 119752.
[10] W. Hu, T. Selleri, F. Gramigni, E. Fenes, K. R. Rout, S. Liu, I. Nova, D. Chen, X. Gao, E. Tronconi, *Ang. Chem. Int. Ed.* **2021**, *60*, 7197–7204.
[11] W. Hu, F. Gramigni, N. D. Nasello, N. Usberti, U. Iacobone, S. Liu, I. Nova, X. Gao, E. Tronconi, *ACS Catal.* **2022**, *12*, 5263–5274.
[12] C. Paolucci, I. Khurana, A. A. Parekh, S. Li, A. J. Shih, H. Li, J. R. Di Iorio, J. D. Albarracin-Caballero, A. Yezerets, J. T. Miller, W. N. Delgass, F. H. Ribeiro, W. F. Schneider, R. Gounder, *Science* **2017**, *357*, 898–903.
[13] A. M. Robles, G. Deplano, K. Góra-Marek, M. Rotko, A. Wach, M. F. Lukman, M. Bertmer, M. Signorile, S. Bordiga, A. Pöppl, R. Gläser, M. Jabłońska, *Catalysts* **2024**, *14*, 457.
[14] R. S. R. Suharbiansah, M. F. Lukman, C. Nannuzzi, A. Wach, K. Góra-Marek, M. Liebau, A. Palčić, A. Pöppl, G. Berlier, S. Bordiga, R. Gläser, M. Jabłońska, *Catal. Sci. Technol.* **2023**, *13*, 3804–3817.
[15] R. Daya, D. Trandal, U. Menon, D. J. Deka, W. P. Partridge, S. Y. Joshi, *ACS Catal.* **2022**, *12*, 6418–6433.
[16] M. Jabłońska, A. M. Robles, M. Rotko, T. H. Vuong, H. Lei, Ž. Lavrič, M. Grilc, M. F. Lukman, R. Valiullin, M. Bertmer, J. Möllmer, J. Rabeah, A. Pöppl, U. Simon, R. Gläser, *ChemSusChem* **2024**, *17*, e202400198.
[17] C. Negri, T. Selleri, E. Borfecchia, A. Martini, K. A. Lomachenko, T. V. W. Janssens, M. Cutini, S. Bordiga, G. Berlier, *JACS* **2020**, *142*, 15884–15896.
[18] J. Abdul Nasir, J. Guan, T. W. Keal, A. W. Desmoutier, Y. Lu, A. M. Beale, C. R. A. Catlow, A. A. Sokol, *JACS* **2022**, *145*, 247–259.
[19] C. Negri, E. Borfecchia, M. Cutini, K. A. Lomachenko, T. V. W. Janssens, G. Berlier, S. Bordiga, *ChemCatChem* **2019**, *11*, 3828–3838.
[20] S. I. Zones, *J. Chem. Soc., Faraday Trans.* **1991**, *87*, 3709–3716.
[21] M. Itakura, T. Inoue, A. Takahashi, T. Fujitani, Y. Oumi, T. Sano, *Chem. Lett.* **2008**, *37*, 908–909.
[22] A. Palčić, P. C. Bruzzese, K. Pyra, M. Bertmer, K. Góra-Marek, D. Poppitz, A. Pöppl, R. Gläser, M. Jabłońska, *Catalysts* **2020**, *10*, 506.
[23] L. Tang, K.-G. Haw, Y. Zhang, Q. Fang, S. Qiu, V. Valtchev, *Microporous. Mesoporous. Mat.* **2019**, *280*, 306–314.

[24] Z. Liu, A. Chokkalingam, S. Miyagi, M. Yoshioka, T. Ishikawa, H. Yamada, K. Ohara, N. Tsunoji, Y. Naraki, T. Sano, T. Okubo, T. Wakihara, *Phys. Chem. Chem. Phys.* **2022**, *24*, 4136–4146.
[25] M. M. J. Treacy, J. B. Higgins, *Collection of simulated XRD powder patterns for zeolites*, 5th revised ed, Elsevier, USA **2007**.
[26] Z. N. Kayani, M. Umer, S. Riaz, S. Naseem, *J. Electron. Mater.* **2015**, *44*, 3704–3709.
[27] M. Thommes, K. Kaneko, A. V. Neimark, J. P. Olivier, F. Rodriguez-Reinoso, J. Rouquerol, K. S. W. Sing, *Pure Appl. Chem.* **2015**, *87*, 1051–1069.
[28] *Zeolites and zeolite-like materials* (Eds: B. Sels, L.M. Kustov), Elsevier, Amsterdam **2016**.
[29] F. Giordanino, P. N. R. Vennestrøm, L. F. Lundegaard, F. N. Stappen, S. Mossin, P. Beato, S. Bordiga, C. Lamberti, *Dalton Trans.* **2013**, *42*, 12741.
[30] D. Nielsen, Q. Gao, T. V. W. Janssens, P. N. R. Vennestrøm, S. Mossin, *J. Phys. Chem. C* **2023**, *127*, 12995–13004.
[31] L. Chmielarz, M. Rutkowska, P. Kuśtrowski, M. Drozdek, Z. Piwowarska, B. Dudek, R. Dziembaj, M. Michalik, *J. Thermal Anal. Calorim.* **2011**, *105*, 161–170.
[32] M. Jabłońska, M. A. Arán, A. M. Beale, K. Góra-Marek, G. Delahay, C. Petitto, K. Pacultová, R. Palkovits, *RSC Adv.* **2019**, *9*, 3979–3986.
[33] P. C. Bruzzese, E. Salvadori, B. Civalleri, S. Jäger, M. Hartmann, A. Pöppl, M. Chiesa, *JACS.* **2022**, *144*, 13079–13083.
[34] A. Godiksen, F. N. Stappen, P. N. R. Vennestrøm, F. Giordanino, S. B. Rasmussen, L. F. Lundegaard, S. Mossin, *J. Phys. Chem. C* **2014**, *118*, 23126–23138.
[35] P. Vanelderen, J. Vancauwenbergh, B. F. Sels, R. A. Schoonheydt, *Coord. Chem. Rev.* **2013**, *257*, 483–494.
[36] F. Gramigni, N. D. Nasello, N. Usberti, U. Iacobone, T. Selleri, W. Hu, S. Liu, X. Gao, I. Nova, E. Tronconi, *ACS Catal.* **2021**, *11*, 4821–4831.
[37] W. Hu, U. Iacobone, F. Gramigni, Y. Zhang, X. Wang, S. Liu, C. Zheng, I. Nova, X. Gao, E. Tronconi, *ACS Catal.* **2021**, *11*, 11616–11625.
[38] C. Liu, S. Yasumura, T. Toyao, Z. Maeno, K. Shimizu, *J. Phys. Chem. C* **2022**, *126*, 11594–11601.
[39] S. Prodinger, M. A. Derewinski, Y. Wang, N. M. Washton, E. D. Walter, J. Szanyi, F. Gao, Y. Wang, C. H. F. Peden, *Appl. Catal. B: Environ.* **2017**, *201*, 461–469.
[40] G. Ramis, L. Yi, G. Busca, M. Turco, E. Kotur, R. J. Willey, *J. Catal.* **1995**, *157*, 523–535.
[41] M. Jabłońska, R. S. R. Suharbiansah, N. Zhang, K. Shimizu, M. F. Lukman, M. Bertmer, H. Lei, A. Pöppl, U. Simon, R. Gläser, *Catal. Today* **2024**, *432*, 114611.
[42] R. S. R. Suharbiansah, K. Pyra, M. Liebau, D. Poppitz, K. Góra-Marek, R. Gläser, M. Jabłońska, *Microporous. Mesoporous. Mat.* **2022**, *334*, 111793.
[43] Y. Feng, X. Wang, T. V. W. Janssens, P. N. R. Vennestrøm, J. Jansson, M. Skoglundh, H. Grönbeck, *ACS Catal.* **2021**, *11*, 14395–14407.
[44] Y. Wang, R. Zhao, K. G. Rappé, Y. Wang, F. Che, F. Gao, *Appl. Catal. B: Environ. Energy.* **2024**, *346*, 123726.
[45] D. Chen, A. Khetan, H. Lei, V. Rizzotto, J.-Y. Yang, J. Jiang, Q. Sun, B. Peng, P. Chen, R. Palkovits, D. Ye, U. Simon, *Environ. Sci. Technol.* **2023**, *57*, 16121–16130.
[46] V. Rizzotto, D. Chen, B. M. Tabak, J.-Y. Yang, D. Ye, U. Simon, P. Chen, *Chemosphere* **2020**, *250*, 126272.
[47] C. Paolucci, A. A. Verma, S. A. Bates, V. F. Kispersky, J. T. Miller, R. Gounder, W. N. Delgass, F. H. Ribeiro, W. F. Schneider, *Ang. Chem. Int. Ed.* **2014**, *53*, 11828–11833.
[48] H. Lei, D. Chen, J. Yang, A. Khetan, J. Jiang, B. Peng, U. Simon, D. Ye, P. Chen, *Environ. Sci. Technol.* **2023**, *57*, 12465–12475.
[49] Y. Fu, W. Ding, H. Lei, Y. Sun, J. Du, Y. Yu, U. Simon, P. Chen, Y. Shan, G. He, H. He, *JACS.* **2024**, *146*, 11141–11151.
[50] J. Yang, X. Li, Y. Xu, L. Chen, S. Wang, S. Ren, J. Zhu, *Appl. Surf. Sci.* **2024**, *647*, 158969.
[51] S. L. Shannon, J. G. Goodwin, *Chem. Rev.* **1995**, *95*, 677–695.
[52] C. Ledesma, J. Yang, D. Chen, A. Holmen, *ACS Catal.* **2014**, *4*, 4527–4547.
[53] C. Fan, Z. Chen, L. Pang, S. Ming, X. Zhang, K. B. Albert, P. Liu, H. Chen, T. Li, *App. Catal. A: Gen.* **2018**, *550*, 256–265.
[54] F. Gao, N. M. Washton, Y. Wang, M. Kollár, J. Szanyi, C. H. F. Peden, *J. Catal.* **2015**, *331*, 25–38.
[55] T. V. W. Janssens, E. Borfecchia, K. A. Lomachenko, H. Grönbeck, G. Berlier, *ChemCatChem* **2024**, *16*, e202400384.
[56] L. Chen, T. V. W. Janssens, H. Grönbeck, *Phys. Chem. Chem. Phys.* **2019**, *21*, 10923–10930.
[57] G. Contaldo, M. Ferri, C. Negri, I. Nova, M. Maestri, E. Tronconi, *ChemCatChem* **2023**, *15*, e202300673.
[58] C. Liu, H. Kubota, T. Toyao, Z. Maeno, K. Shimizu, *Catal. Sci. Technol.* **2020**, *10*, 3586–3593.

Manuscript received: June 23, 2025
Revised manuscript received: September 16, 2025
Accepted manuscript online: September 16, 2025
Version of record online: ■■, ■■